Elliptical Silicon Nanowire Covered by the SEI in a 2D Chemo–Mechanical Simulation

Raphael Schoof,*,+,[a] Lukas Köbbing,*,+,[b,c] Arnulf Latz,[b,c,d] Birger Horstmann,[b,c,d] Willy Dörfler[a]

Understanding the mechanical interplay between silicon anodes and their surrounding solid-electrolyte interphase (SEI) is essential to improve the next generation of lithium-ion batteries. We model and simulate a 2D elliptical silicon nanowire with SEI via a thermodynamically consistent chemo-mechanical continuum ansatz using a higher order finite element method in combination with a variable-step, variable-order time integration scheme. Considering a soft viscoplastic SEI for three half cycles, we see at the minor half-axis the largest stress magnitude at the silicon nanowire surface, leading to a concentration anomaly. This anomaly is caused by the shape of the nanowire itself and not by the SEI. Also for the tangential stress of the SEI, the largest stress magnitudes are at this point, which can lead to SEI fracture. However, for a stiff SEI, the largest stress magnitude inside the nanowire occurs at the major half-axis, causing a reduced concentration distribution in this area. The largest tangential stress of the SEI is still at the minor half-axis. In total, we demonstrate the importance of considering the mechanics of the anode and SEI in silicon anode simulations and encourage further numerical and model improvements.

1. Introduction

Silicon anodes can present the next vital step towards improved lithium-ion batteries with higher capacity [1–5]. Nevertheless, the significant ability for lithiation causes massive volume changes during cycling, hindering the commercialization of pure silicon anodes [6, 7]. The substantial deformations lead to mechanical instabilities of anode particles larger than 150 nm and cause particle fracture and pulverization [8, 9]. Consequently, hopes are pinned on nanostructured silicon anodes [10–12] and silicon nanowires in particular [13–15].

Due to electrolyte instability in contact with anode particles, the solid-electrolyte interphase (SEI) forms on silicon anodes, reasonably passivating the electrolyte from further decomposition [16–19]. However, the SEI continues to grow during storage and battery operation via electron transport from the anode towards the electrolyte [20–22]. On silicon anodes, the SEI and its mechanical behavior merit special attention as the massive volume changes of the anode challenge the stability of the SEI [23, 24]. Nonetheless, the inner SEI is reported to stay intact during cycling [25]. Thus, it is important to consider the stress generated inside the SEI and its implication for silicon anodes in simulations of the silicon-SEI system [26–28].

Our previous works discussed the silicon-SEI system with spherical symmetry [24, 26, 27, 29]. Additionally, we performed 2D simulations of the nanowire only [30–32] and restricted expansion by a rigid obstacle [33]. As literature reports the importance of non-symmetric geometries on the mechanical properties during cycling [34] in contrast to a spherical setup [35], we investigate the mechanics of an elliptical silicon nanowire covered by SEI in this manuscript. Therefore, we straightforwardly adapt our 1D radial symmetric setup for the chemical and elastic silicon core as well as the elastic and viscoplastic SEI shell to the 2D elliptical nanowire. Our variable-step, variable-order time integration scheme is combined with a higher order finite element method. In total, we simulate three half cycles, meaning a first lithiation is followed by delithiation and a second lithiation. We provide extensive investigations of the mechanical characteristics and concentration distribution for the coupled silicon-SEI structure.

The remaining of this manuscript is structured as follows: in section 2, we present the key details of our continuum modeling, followed by a brief summary of our numerical procedure in section 3. The focus of this work is section 4, in which we present our extensive numerical results and discussions. We conclude with a summary and a short outlook in section 5.

2. Theory

We follow Ref. [29] and briefly recap our chemo-mechanically coupled model for the *silicon-SEI* approach. This ansatz is based on the thermodynamically consistent theory by Refs. [24, 26, 29–31, 36, 37].

We use a purely elastic (Lagrangian) logarithmic Hencky strain for the finite deformation model of the electrode nanowire, whereas we apply a viscoplastic approach for the SEI. For a purely elastic particle without SEI, the typically used Lagrangian strain or Green–St-Venant strain leads to similar results compared to the Hencky strain [31, 38]. The

[a] R. Schoof, Prof. Dr. W. Dörfler
Karlsruhe Institute of Technology (KIT), Institute for Applied and Numerical Mathematics, Englerstraße 2, 76131 Karlsruhe, Germany
E-mail: raphael.schoof@kit.edu

[b] L. Köbbing, Prof. Dr. A. Latz, Prof. Dr. B. Horstmann
German Aerospace Center (DLR), Wilhelm-Runge-Straße 10, 89081 Ulm, Germany
E-mail: lukas.koebbing@dlr.de

[c] L. Köbbing, Prof. Dr. A. Latz, Prof. Dr. B. Horstmann
Helmholtz Institute Ulm (HIU), Helmholtzstraße 11, 89081 Ulm, Germany

[d] Prof. Dr. A. Latz, Prof. Dr. B. Horstmann
Faculty of Natural Sciences, Ulm University, Albert-Einstein-Allee 47, 89081 Ulm, Germany
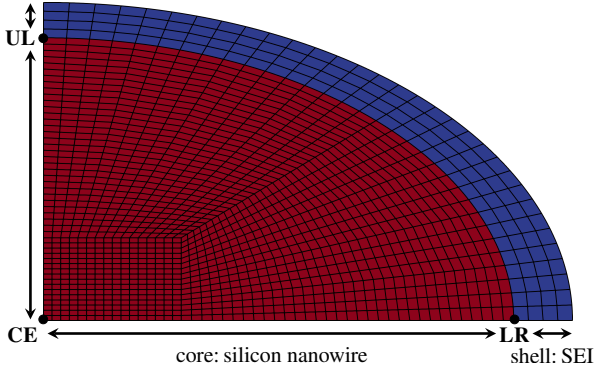
[+] These authors contributed equally.

Figure 1. Sketch of the silicon nanowire core (red) covered by the SEI shell (blue) with the underlying time-constant computational grid and the points **LR** (lower right), **UL** (upper left) and **CE** (center) for further investigations.

deformation Φ relates the reference (Lagrangian) configuration $\Omega_0 \subset \mathbb{R}^3$ to the current (Eulerian) configuration Ω. A silicon core subdomain and a SEI shell subdomain are identified in each frame, indicated with the subscript C and S, respectively. In this work, we consider a quarter section of an elliptical nanowire, resulting from symmetry assumptions along both half-axes as well as free expansion and vanishing stresses in the third direction. At the half-axes, we impose a non-displacement condition in tangential direction. A sketch of the considered domain with the underlying computational grid is depicted in Figure 1.

Finite Deformation. The deformation gradient $\mathbf{F} = \mathbf{Id} + \boldsymbol{\nabla}_0 \boldsymbol{u}$ with the identity tensor $\mathbf{Id}$ and the displacement vector $\boldsymbol{u}$ can be split up multiplicatively into three parts: $\mathbf{F} = \mathbf{F}_{\mathrm{ch}}\mathbf{F}_{\mathrm{el}}\mathbf{F}_{\mathrm{pl}}$, the chemical, elastic, and plastic deformation, respectively, compare Sect. 10.4 in Ref. [39], Sect. 8.2.2 in Ref. [40] and Ref. [41].

In the silicon core domain, we consider only reversible deformations $\mathbf{F} = \mathbf{F}_{\mathrm{ch}}\mathbf{F}_{\mathrm{el}} = \mathbf{F}_{\mathrm{rev}}$. The elastic part results from mechanical stresses and the chemical part from changes of the lithium concentration during lithiation and delithiation as $\mathbf{F}_{\mathrm{ch}} = \lambda_{\mathrm{ch}}\mathbf{Id} = \sqrt[3]{1 + v_{\mathrm{pmv}}c_{\mathrm{max}}\bar{c}}\,\mathbf{Id}$ with the partial molar volume v_{pmv} of lithium inside silicon, the normalized lithium concentration $\bar{c} = c/c_{\mathrm{max}} \in [0,1]$ of the lithium concentration $c \in [0, c_{\mathrm{max}}]$ with respect to the maximal concentration c_{max} in the reference configuration. In the SEI domain, no chemical deformation occurs: $\mathbf{F} = \mathbf{F}_{\mathrm{el}}\mathbf{F}_{\mathrm{pl}}$. We omit the index C or S for reasons of better readability if it is clear from the context which part is referred to.

Free Energy. We consider all model equations in the reference configuration at constant temperature and state the Helmholtz free energy $\psi(\bar{c}, \boldsymbol{\nabla}_0 \boldsymbol{u}, \mathbf{F}_{\mathrm{pl}}) = \psi_{\mathrm{ch}}(\bar{c}) + \psi_{\mathrm{el}}(\bar{c}, \boldsymbol{\nabla}_0 \boldsymbol{u}, \mathbf{F}_{\mathrm{pl}})$ resulting in $\psi(\bar{c}, \boldsymbol{\nabla}_0 \boldsymbol{u}_{\mathrm{C}}) = \psi_{\mathrm{ch}}(\bar{c}) + \psi_{\mathrm{el}}(\bar{c}, \boldsymbol{\nabla}_0 \boldsymbol{u}_{\mathrm{C}})$ and $\psi(\boldsymbol{\nabla}_0 \boldsymbol{u}_{\mathrm{S}}, \mathbf{F}_{\mathrm{pl}}) = \psi_{\mathrm{el}}(\boldsymbol{\nabla}_0 \boldsymbol{u}_{\mathrm{S}}, \mathbf{F}_{\mathrm{pl}})$ for the respective silicon core and SEI shell domain. With the mass density ρ_0 of silicon in the reference configuration the chemical and elastic free energy densities can be defined as

$$\rho_0 \psi_{\mathrm{ch}}(\bar{c}) = -c_{\mathrm{max}} \int_0^{\bar{c}} F\, U_{\mathrm{OCV}}(z)\, \mathrm{d}z$$

with an experimental open-circuit voltage (OCV) curve U_{OCV} [24, 26, 31, 33] and the Faraday constant F as well as

$$\rho_0 \psi_{\mathrm{el}}(\bar{c}, \boldsymbol{\nabla}_0 \boldsymbol{u}, \mathbf{F}_{\mathrm{pl}}) = \frac{1}{2}\mathbf{E}_{\mathrm{el}}(\bar{c}, \boldsymbol{\nabla}_0 \boldsymbol{u}, \mathbf{F}_{\mathrm{pl}}) : \mathbb{C}[\mathbf{E}_{\mathrm{el}}]$$

with $\mathbf{F}_{\mathrm{pl}} = \mathbf{Id}$ for silicon, the elastic strain tensor $\mathbf{E}_{\mathrm{el}}$, and the constant, isotropic stiffness fourth-order tensor $\mathbb{C}$ as $\mathbb{C}[\mathbf{E}_{\mathrm{el}}] = \lambda \operatorname{tr}(\mathbf{E}_{\mathrm{el}})\,\mathbf{Id} + 2G\mathbf{E}_{\mathrm{el}}$. Here, $\lambda = 2G\nu/(1-2\nu)$ and $G = E/(2(1+\nu))$ are the first and second Lamé constants, respectively, depending further on Young's modulus E and Poisson's ratio ν. In Table 1, we give the parameters for silicon and SEI. The (Lagrangian) logarithmic Hencky strain tensor $\mathbf{E}_{\mathrm{el}}$ is given as $\mathbf{E}_{\mathrm{el}} = \ln(\mathbf{U}_{\mathrm{el}}) = \ln(\sqrt{\mathbf{C}_{\mathrm{el}}}) = \sum_{\alpha=1}^3 \ln(\sqrt{\eta_{\mathrm{el},\alpha}})\,\boldsymbol{r}_{\mathrm{el},\alpha} \otimes \boldsymbol{r}_{\mathrm{el},\alpha}$ with the eigenvalues $\eta_{\mathrm{el},\alpha}$ and eigenvectors $\boldsymbol{r}_{\mathrm{el},\alpha}$ of $\mathbf{U}_{\mathrm{el}}$. The tensor $\mathbf{U}_{\mathrm{el}}$ is the unique, symmetric and positive definite right stretch part of the unique polar decomposition of $\mathbf{F}_{\mathrm{el}} = \mathbf{R}_{\mathrm{el}}\mathbf{U}_{\mathrm{el}}$, see Sect. 2.6 in Ref. [42].

Chemistry. The lithium concentration changes during lithiation and delithiation inside the reference silicon core domain $\Omega_{0,\mathrm{C}}$ can be stated via a generalized diffusivity equation [24, 43, 44]

$$\partial_t c = -\boldsymbol{\nabla}_0 \cdot \boldsymbol{N}. \tag{1}$$

The lithium flux $\boldsymbol{N} = -D\,(\partial_c\mu)^{-1}\,\boldsymbol{\nabla}_0\mu$ with the diffusion coefficient D for lithium in silicon is applied for an isotropic case. The chemical potential μ can be derived as the partial derivative of the free energy density with respect to the concentration c [24, 26, 31, 33, 36]

$$\mu = \partial_c(\rho_0\psi) = \mu_{\mathrm{ch}} + \mu_{\mathrm{el}}$$
$$= -F\,U_{\mathrm{OCV}} - \frac{v_{\mathrm{pmv}}}{3\lambda_{\mathrm{ch}}^3}\operatorname{tr}(\mathbb{C}[\mathbf{E}_{\mathrm{el}}]). \tag{2}$$

Therefore, the total lithium flux $\boldsymbol{N} = \boldsymbol{N}_{\mathrm{ch}} + \boldsymbol{N}_{\mathrm{el}}$ can be divided into the lithium concentration-driven diffusive flux component $\boldsymbol{N}_{\mathrm{ch}} = -D\,(\partial_c\mu)^{-1}\,\boldsymbol{\nabla}_0\mu_{\mathrm{ch}}$ and the stress-driven convective flux component $\boldsymbol{N}_{\mathrm{el}} = -D\,(\partial_c\mu)^{-1}\,\boldsymbol{\nabla}_0\mu_{\mathrm{el}}$, respectively. A uniform and constant external flux N_{ext} in the Lagrangian domain with either positive or negative sign (for lithiation or delithiation, respectively) is applied at the surface of the silicon core. This external flux is measured with regard to the charging rate (C-rate) connecting the state of charge (SOC) to the simulation time via the external lithium flux and the initial concentration $\mathrm{SOC}(t) = \bar{c}_0 + N_{\mathrm{ext}}t$. Further information about the SOC, the C-rate and N_{ext} can be found in Refs. [24, 30, 31] and the references cited therein.

Elastic and Inelastic Deformation. We solve the momentum balance equation [24, 30, 31, 33] in the silicon core domain and the SEI shell domain

$$\mathbf{0} = \boldsymbol{\nabla}_0 \cdot \mathbf{P}_{\mathrm{C}}(\bar{c}, \boldsymbol{\nabla}_0\boldsymbol{u}_{\mathrm{C}}), \qquad \mathbf{0} = \boldsymbol{\nabla}_0 \cdot \mathbf{P}_{\mathrm{S}}(\boldsymbol{\nabla}_0\boldsymbol{u}_{\mathrm{S}}, \mathbf{F}_{\mathrm{pl}}) \tag{3}$$

for the respective deformation. The first Piola–Kirchhoff tensor $\mathbf{P}$ is thermodynamically consistently derived as

$$\mathbf{P} = 2\mathbf{F}\partial_{\mathbf{C}}(\rho_0\psi) = \mathbf{F}\left(\mathbf{F}_{\mathrm{el}}^{\mathsf{T}}\mathbf{F}_{\mathrm{el}}\right)^{-1}\left(\mathbf{F}_{\mathrm{pl}}^{-1}\right)^{\mathsf{T}}\mathbf{F}_{\mathrm{pl}}^{-1}\mathbb{C}[\mathbf{E}_{\mathrm{el}}],$$

see Refs. [24, 26, 31, 33]. With the first Piola–Kirchhoff tensor $\mathbf{P}$ we state the related symmetric Cauchy stress $\boldsymbol{\sigma}$ in the current configuration as $\boldsymbol{\sigma} = \mathbf{P}\mathbf{F}^{\mathsf{T}}/\det(\mathbf{F})$, see Sect. 3.1 in Ref. [42].

In this work, we rely on the rate-dependent plastic approach [29, 31]. Therefore, we introduce the scalar yield stress σ_{Y} and the evolution equation of the scalar accumulated equivalent inelastic strain $\varepsilon_{\mathrm{pl}}^{\mathrm{eq}} \geq 0$ as

$$\dot{\varepsilon}_{\mathrm{pl}}^{\mathrm{eq}} = \begin{cases} 0, & \|\mathbf{M}^{\mathrm{dev}}\| \leq \sigma_{\mathrm{Y}}, \\ \dot{\varepsilon}_0\left(\dfrac{\|\mathbf{M}^{\mathrm{dev}}\| - \sigma_{\mathrm{Y}}}{\sigma_{\mathrm{Y}^*}}\right)^{\beta}, & \|\mathbf{M}^{\mathrm{dev}}\| > \sigma_{\mathrm{Y}}, \end{cases}$$

which replace the typical Karush–Kuhn-Tucker (KKT) conditions for the plastic approach, compare Sect. 1.7 in Ref. [45] and Refs. [29, 31, 41]. The deviatoric Mandel stress $\mathbf{M}^{\mathrm{dev}} = \mathbf{M} - 1/3\,\mathrm{tr}(\mathbf{M})\,\mathbf{Id}$ is computed via the Mandel stress $\mathbf{M} = \partial_{\mathbf{E}_{\mathrm{el}}}(\rho_0 \psi_{\mathrm{el}}) = \mathbb{C}_{\mathrm{S}}[\mathbf{E}_{\mathrm{el}}]$ in the SEI domain. The remaining values are the positive-valued stress-dimensioned constant σ_{Y^*}, the reference tensile stress $\dot{\varepsilon}_0$, and the measure of the strain rate sensitivity of the material β which are given in Table 1. Furthermore, we rescale the yield stress with the factor $\sqrt{2/3}$ due to consistency with the one dimensional tensile test, see Sect. 2.3.1 in Ref. [45]. Finally, we use a projector formulation to map the stresses onto the set of admissible stresses, stated for our viscoplastic approach in Ref. [31]. This procedure is also known as static condensation [46, 47]. Therefore, $\mathbf{F}_{\mathrm{pl}}$ and $\varepsilon_{\mathrm{pl}}^{\mathrm{eq}}$ are applied as internal variables. This procedure has the advantage that the nonlinear system of partial differential equations does not need to be extended by the plastic part of the deformation gradient, in contrast to Refs. [24, 26].

3. Numerical Approach

Again, we follow Ref. [29] and state only the most important details. All in all, after non-dimensionalization and omitting the accentuation for the non-dimensionalization, we solve for given $\mathbf{F}_{\mathrm{pl}}$ and $\varepsilon_{\mathrm{pl}}^{\mathrm{eq}}$ the continuity equation in Eq. 1, the chemical potential equation in Eq. 2, and the momentum balance equations in Eq. 3. As a result, we obtain the concentration c, the chemical potential μ, and the silicon core displacement $\boldsymbol{u}_{\mathrm{C}}$ as well as the SEI shell displacement $\boldsymbol{u}_{\mathrm{S}}$. Therefore, we imply boundary conditions at the interface between the silicon core and the SEI shell domain: $\boldsymbol{u}_{\mathrm{C}} = \boldsymbol{u}_{\mathrm{S}}$ and $\mathbf{P}_{\mathrm{C}} \cdot \boldsymbol{n} = \mathbf{P}_{\mathrm{S}} \cdot \boldsymbol{n}$ with the normal vector $\boldsymbol{n} = \boldsymbol{n}_{\mathrm{C}}$. At the outer boundary of the SEI, we have no stresses meaning $\mathbf{P}_{\mathrm{S}} \cdot \boldsymbol{n}_{\mathrm{S}} = \mathbf{0}$. Furthermore, we impose initial conditions $c(0, \cdot) = c_0$, $\mathbf{F}_{\mathrm{pl}}(0, \cdot) = \mathbf{Id}$ and $\varepsilon_{\mathrm{pl}}^{\mathrm{eq}}(0, \cdot) = 0$.

For the numerical solution of the nonlinear system of partial differential equations, we choose an admissible mesh for the computational domain, use the isoparametric Lagrangian finite element method, see Chapt. III §2 in Ref. [48], derive a weak formulation and a spatial and temporal discretization [29]. For the spatial discretization, we apply a fourth order finite element approach using a uniform and time-constant mesh in the reference configuration, displayed in Figure 1. Note that the original set of equations is derived in 3D, however, all equations are also mathematically valid in 2D [30, 31]. The temporal discretization is realized with a variable-step, variable-order time integration scheme using the numerical differential formulation (NDF) of linear multistep methods [49–51]. The temporal discretization of the internal variables are treated with an implicit exponential map. For a detailed procedure of the temporal integration for $\mathbf{F}_{\mathrm{pl}}$ and $\varepsilon_{\mathrm{pl}}^{\mathrm{eq}}$, we refer to Ref. [31]. In each time step, the nonlinear system is solved using the Newton–Raphson method and the adaptive scheme for the time presented as Algorithm 1 in Ref. [30].

We start with the constant initial concentration $\bar{c}_0 = 0.02$ and $\mu_0 = \partial_c \rho \psi_{\mathrm{ch}}(\bar{c}_0)$. The initial time step size is $10^{-8}\,\mathrm{h}$, the maximal time step size $10^{-3}\,\mathrm{h}$ and temporal relative and absolute tolerances $2 \cdot 10^{-4}$ and $2 \cdot 10^{-7}$, respectively. The grid has around $87 \cdot 10^3$ degrees of freedom. Additional zero-displacement boundary conditions are applied on the major half-axis with $u_y = 0$ and on the minor half-axis with $u_x = 0$. The Newton update is computed with an LU-decomposition from the UMFPACK package [52, Version 5.7.8] and shared memory with OpenMP Version 4.5 is enabled for assembling the Newton method. Our implementation is based on the open-source finite element library *deal.II* [53]. All simulations are performed on a single node at the BwUniCluster2.0 with GCC 12.1 [54].

4. Results and Discussion

Due to the importance of mechanics and the silicon anode geometry, we investigate the chemo-mechanical coupling of an elliptical silicon nanowire covered by the SEI in a 2D setup. We discuss the stresses occurring inside the silicon anode and the SEI in comparison to a symmetric nanowire. Additionally, we examine the lithium concentration distribution and gradients during lithiation and delithiation influenced by mechanics. To assess the impact of the SEI, we compare the chemo-mechanical results for a silicon anode covered by a soft and a stiff SEI layer.

During cycling, the lithium concentration inside the silicon nanowire changes. An increase in the lithium concentration results in a chemical expansion of the anode, while a decrease leads to a shrinkage. Inhomogeneous lithium distribution inside the silicon implies inhomogeneous volume changes that have to be accommodated by mechanical deformations. These mechanical strains inside the lithiated silicon generate stresses. While the silicon can deform chemically and elastically, the SEI features elastic and viscoplastic material behavior. During cycling, the SEI layer has to adjust to the volume changes of the silicon anode. As the SEI can only deform mechanically, expansion and shrinkage of the silicon anode lead to significant mechanical strains, creating stresses inside the SEI as well. The stresses inside silicon and SEI are coupled due to the interface condition of equal stress in normal direction.

4.1. Silicon Nanowire with Soft SEI

First, we investigate the behavior of an elliptical silicon nanowire covered by a soft SEI layer. The ratio of the minor to the major half-axis is 0.6:1. The SEI thickness is one eighth of the silicon core length. We simulate three half cycles (1st lithiation, 1st delithiation, and 2nd lithiation) with a rate of 1 C. The simulation parameters are stated in Table 1. We begin our discussion with the mechanics inside the silicon anode and the SEI layer and continue with the examination of the lithium concentration distribution. Especially, we consider the quantities of interest at the lower right of the major half-axis (point **LR**), at the upper left of the minor half-axis (point **UL**), and at the center of the silicon (point **CE**), respectively. The interfacial points (**LR** and **UL**) and the central point (**CE**) are illustrated in Figure 1.

Concerning the mechanics inside the silicon anode, lithiation from the outside leads to concentration gradients and inhomogeneous volume changes. The volume mismatch generates compressive stress at the outer boundary of the nanowire and tensile stress at the center. During delithiation, lithium flux out of the anode leads to tensile stress at the outer boundary and compressive stress at the center. To investigate the mechanics in detail, we illustrate the simulated stresses for the elliptical silicon nanowire covered by a soft SEI layer in Figure 2. We depict the stress distribution during lithiation at 30% SOC for the normal component σ_{n}
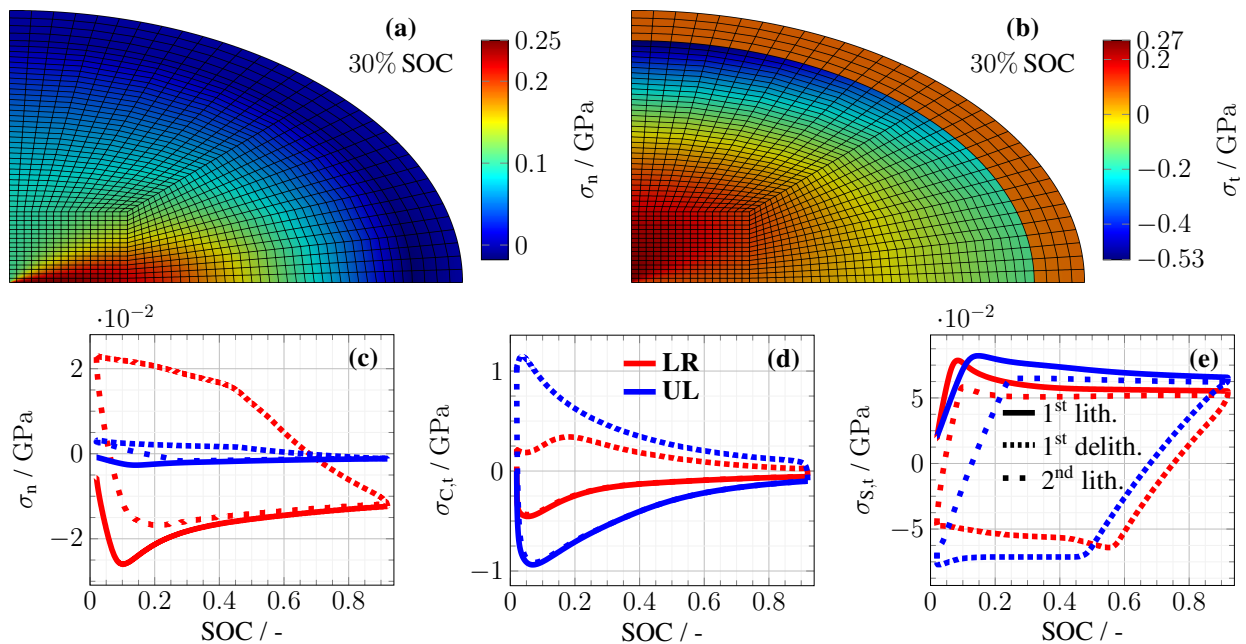
Figure 2. Cauchy stresses for the elliptical silicon nanowire with a soft SEI. Distribution of (a) normal and (b) tangential Cauchy stress inside the silicon core and the SEI shell during lithiation at 30% SOC. Evolution of Cauchy stress at the points **LR** and **UL** during three half cycles for (c) normal, (d) tangential core, and (e) tangential shell stress.

in Figure 2(a) and the tangential component σ_t in Figure 2(b). Both stress distributions reveal the general trend of tensile stress at the center and compressive stress at the outer boundary of the silicon nanowire. The largest compressive stresses appear in normal direction at the end of the major half-axis at point **LR** and in tangential direction at the end of the minor half-axis at point **UL**. The largest tensile stresses appear in normal direction along the major half-axis and in tangential direction along the minor half-axis, each close to the center. Therefore, possible plasticity [31] and fracture might occur along the minor half-axis.

We depict the time evolution of the stress inside silicon during three half cycles for the normal component in Figure 2(c) and for the tangential component in Figure 2(d). The evolution of the stress components during the first lithiation reveals permanent compressive stress at points **UL** and **LR**, with significantly larger stress magnitudes for the tangential component. The normal stress in Figure 2(c) always shows the largest magnitude at the major half-axis at point **LR**, and the tangential stress in Figure 2(d) shows the largest magnitude at the minor half-axis at point **UL**. During the subsequent delithiation, tensile stresses arise at the outer boundary, showing the largest magnitudes at the same points as before. The normal stress during the second lithiation in Figure 2(c) deviates from the first lithiation in the beginning due to a different initial state, but the stresses continuously approach the ones during the first lithiation. The tangential stress during the second lithiation in Figure 2(d) coincides with the first lithiation. The largest stress magnitudes during cycling occur at low SOC in particular in tangential direction at the end of the minor half-axis at point **UL**. This supports our previous finding that the elliptical silicon nanowire might be prone to plasticity [31] and fracture in this regime.

To highlight the influence of the elliptical geometry, we compare our simulation results to the case of a symmetric silicon nanowire with the same capacity in Figure 6. Due to the symmetry, the stresses at points **UL** and **LR** are equal. The stress magnitudes of the normal and tangential stress components at the outer boundary in the symmetric case are always in between the stress values at point **UL** and **LR** for the elliptical case. Therefore, the largest stresses reached during cycling in the symmetric case stay smaller than the ones for the elliptical case. Consequently, the symmetric silicon nanowires are mechanically more stable than elliptical silicon nanowires with the same capacity.

Next, we discuss the mechanics of the SEI shell during cycling. The Cauchy stress in normal direction in silicon and SEI is coupled at the interface. At the outer boundary of the SEI, the stress in normal direction vanishes. Therefore, we focus on the description of the tangential component of the SEI stress depicted in Figure 2(e). During lithiation, the volume expansion of the nanowire leads to tensile tangential stress inside the SEI. The tangential stress magnitude at the minor half-axis at point **UL** is slightly larger compared to point **LR**. This can be expected as the curvature of the SEI is smallest at the end of the minor half-axis. Thus, the SEI might be prone to fracture at point **UL**. During delithiation, the tangential stress inside the SEI is compressive and the maximum value is reached again at point **UL**. During the second lithiation, the size of the stress overshoot reduces and the stress converges to that one of the first lithiation. Compared to the symmetric nanowire, we observe the same trend for the stresses inside the SEI shell as for the silicon core. The stress magnitudes are in between the stresses at points **UL** and **LR**. Consequently, the maximum value is smaller for the symmetric case, meaning a superior mechanical stability of the SEI. To investigate the influence of viscosity, we vary the parameter for the plastic strain rate $\dot{\varepsilon}_0$ in Figure 8. A smaller value retards plastic flow, leading to a larger stress overshoot and larger stress magnitudes in general. Nevertheless, the shape of the stress profiles does not change significantly upon variation of $\dot{\varepsilon}_0$.

After the mechanical description, we investigate the lithi-
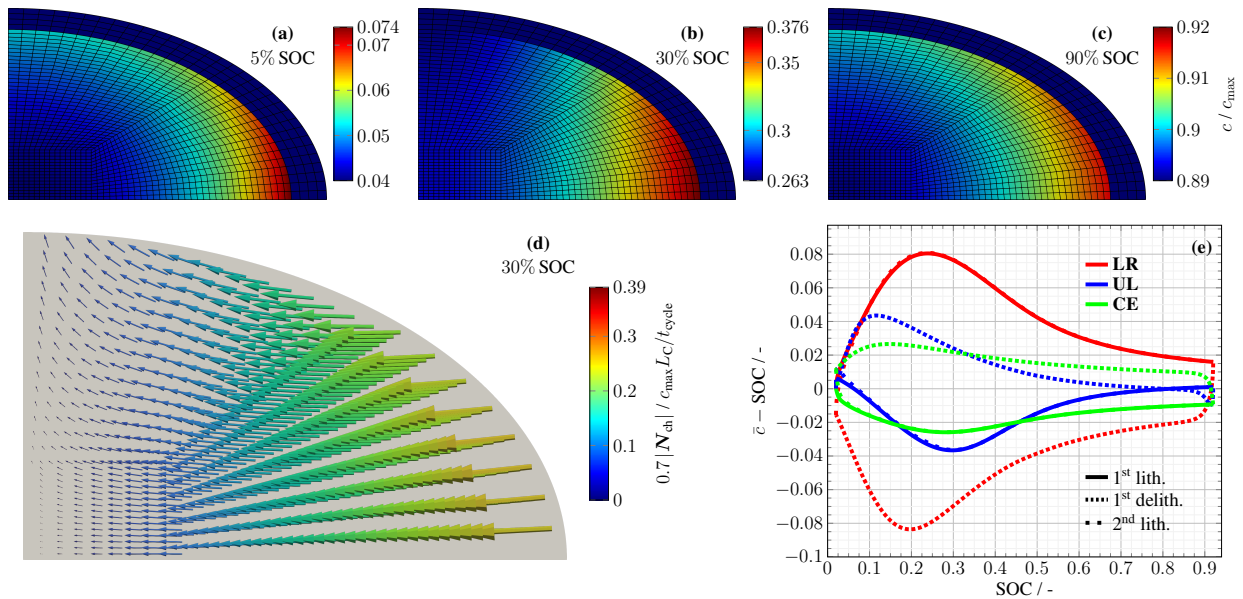
Figure 3. Lithium concentration for the elliptical silicon nanowire with a soft SEI. Distribution of the lithium concentration inside silicon during lithiation at (a) 5%, (b) 30%, and (c) 90% SOC. (d) Concentration-driven diffusive lithium flux N_{ch} scaled with 0.7. (e) Deviation of the lithium concentration from the mean at the points **LR**, **UL**, and **CE** during three half cycles.

um concentration inside the elliptical silicon nanowire. During lithiation, the lithium flux points from the outside into the interior of the silicon anode. Thus, we expect that the concentration at the outer boundary of the anode exceeds the concentration at the center, as shown for the symmetrical nanowire covered by SEI in Figure 7. During delithiation, we expect a decreased lithium concentration at the outer boundary compared to the center. We show our simulation results for the lithium concentration in Figure 3. The lithium distribution inside the elliptical silicon nanowire during lithiation is illustrated in Figure 3(a) to (c) for 5%, 30%, and 90% SOC. As expected, the lithium concentration increases in general from the outside. The lithium distribution reveals the highest concentration at the end of the major half-axis at point **LR**. At this point, the elliptical geometry has the highest local surface-to-volume ratio, resulting in faster lithium concentration increase, compare Section 2.2.3 [55]. Contrary to our expectation, the lithium concentration at the end of the minor half-axis at point **UL** is lower than the concentration at the center point **CE** during lithiation at 30% SOC. For a better illustration of this concentration anomaly, we depict the concentration-driven diffusive lithium flux N_{ch} during lithiation at 30% SOC in Figure 3(d), indicating negatively scaled concentration gradients. Along the major half-axis, lithium diffusion points towards the center of the ellipse, as expected. However, along the minor half-axis, diffusion points towards the outer boundary of the nanowire, revealing the concentration depletion at point **UL**. While the arrows indicating the direction of lithium diffusion partially point towards the outer boundary, the more pronounced stress-driven convective lithium flux N_{el} depicted in Figure 9(a) points towards the interior. This ensures that the total flux N always points towards the interior of the silicon core during lithiation.

To confirm the appearance of the concentration anomaly, we examine the deviation of the lithium concentration from the mean during cycling in Figure 3(e). As expected during lithiation, the concentration at point **LR** is always larger,

and at point **CE** smaller than the mean concentration. During delithiation, this concentration distribution is inverse. However, the concentration at point **UL** is smaller than the mean concentration and even smaller than the concentration in the center **CE** during lithiation in a wider SOC regime between 15% and 45% SOC. The concentration anomaly at point **UL** also appears during delithiation as concentration excess between 35% and 5% SOC and the second lithiation again as depletion. Thus, the concentration anomaly at point **UL** is no simulation artifact in a narrow SOC range during the first lithiation but significant and robust during cycling.

The concentration anomaly also appears during slow cycling with C/20 and inside an elliptical silicon nanowire without SEI as shown in Figure 11. Thus, we exclude kinetic limitations or the mechanical impact of the SEI on the silicon core as reasons for the concentration anomaly. Instead, we attribute this effect to a mechanical origin inside the elliptical silicon nanowire. During lithiation, the lithium concentration increases the fastest at point **LR** at the end of the major half-axis due to the highest surface-to-volume ratio. The significant increase causes pronounced volume expansion, leading to compressive stress along the outer boundary of the nanowire. This compressive stress is largest at point **UL** at the end of the minor half-axis due to the smaller curvature at this point. The substantial compressive stress affects the chemo-mechanical potential and hinders further lithium concentration increase at point **UL**. During delithiation, the fastest decrease in concentration appears at point **LR**, generating tensile stress, especially at point **UL**. The substantial tensile stress impedes lithium concentration decrease at point **UL**, generating a local concentration excess. Investigating a purely chemical 2D elliptical silicon nanowire without mechanical coupling, such a concentration anomaly does not occur. Thus, the concentration anomaly during cycling results from the chemo-mechanical interplay inside the silicon nanowire significantly influenced by the elliptical geometry.
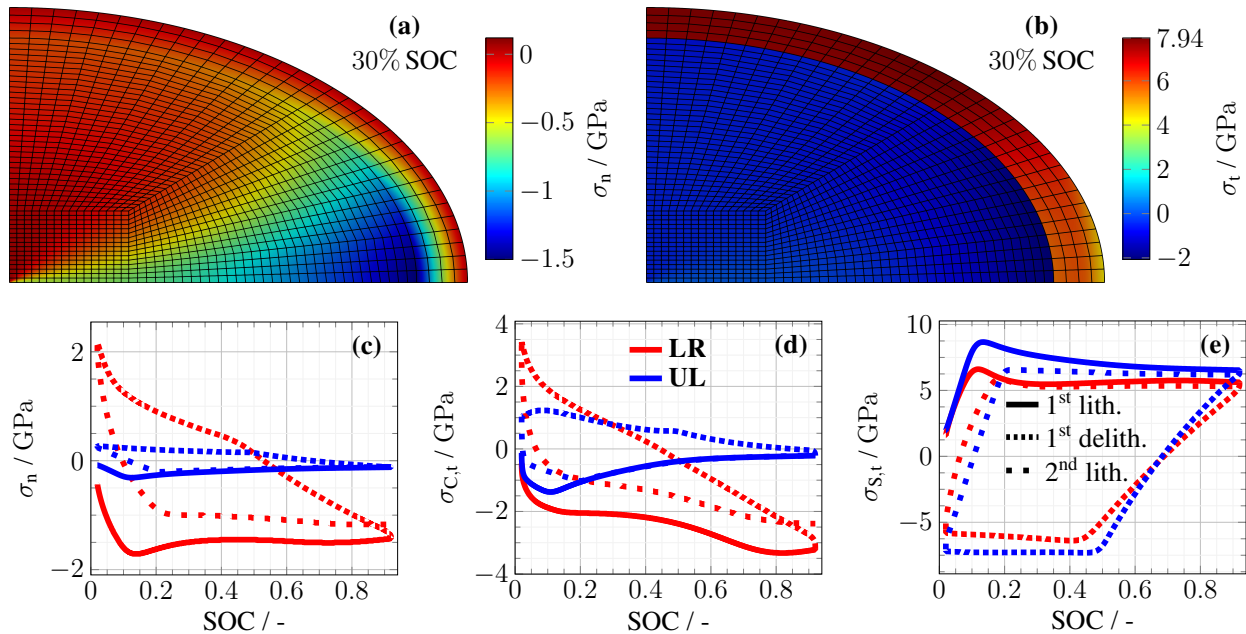
Figure 4. Cauchy stresses for the elliptical silicon nanowire with a stiff SEI. Distribution of (a) normal and (b) tangential Cauchy stress inside the silicon core and the SEI shell during lithiation at 30% SOC. Evolution of Cauchy stress at the points **LR** and **UL** during three half cycles for (c) normal, (d) tangential core, and (e) tangential shell stress.

4.2. Silicon Nanowire with Stiff SEI

After discussing the soft SEI, we want to investigate the influence of a stiff SEI layer on the mechanics and the lithiation behavior of an elliptical silicon nanowire as discussed for a spherical nanoparticle in Ref. [26]. Therefore, we increase the value of Young's modulus and the yield stress of the SEI shell by a factor of 100 compared to the soft SEI, i.e. $E = 90\,\text{GPa}$ and $\sigma_Y = \sigma_{Y*} = 4.95\,\text{GPa}$. The increase in the mechanical parameters immediately evokes elevated stresses inside the SEI. We depict the stress distribution in Figure 4(a) for the normal component and in Figure 4(b) for the tangential component at 30% SOC during lithiation. Analog to the soft SEI scenario, the largest compressive stress in the SEI in normal direction occurs at the major half-axis at point **LR** and the largest tensile stress in tangential direction appears at the minor half-axis at point **UL** due to the local curvature effects. Therefore, possible cracking of the SEI might occur again at point **UL** due to the largest tangential stresses.

The time evolution during cycling of the normal stress in Figure 4(c) and the tangential stress in Figure 4(e) confirms this observation. During delithiation, we observe the largest tensile stress in normal direction inside the SEI at the major half-axis at point **LR** and the largest compressive stress in tangential direction at the minor half-axis at point **UL** accordingly. The stresses during the second lithiation approach the stresses during the first lithiation but deviate due to the viscoplastic behavior. The comparison to the soft SEI case reveals a stress increase inside the SEI for both components by approximately a factor of 100, representing the increase in the mechanical parameters.

The stress inside the silicon nanowire is affected by the stiff SEI layer due to the mechanical coupling of the silicon core and the SEI shell. We depict the normal stress component inside silicon and SEI during lithiation at 30% SOC in Figure 4(a). The illustration reveals that the normal stresses at the interface are equal as imposed by the boundary condi-

tion. The stress distribution shows significantly larger compressive stresses within the whole silicon nanowire except a small region along the minor half-axis close to the center, where tensile stresses appear. Compared to the soft SEI, the most significant normal compressive stress occurs again at the end of the major half-axis at point **LR** due to the largest curvature and pronounced impact of the SEI. The tangential stress component inside silicon depicted in Figure 4(b) is indirectly affected by the different SEI mechanics. The stress distribution reveals compressive stresses within the whole silicon nanowire with the largest stress magnitude at the end of the major half-axis at point **LR**. This is in contrast to the case with the soft SEI, where the largest compressive stress occurs at the end of the minor half-axis at point **UL** and where tensile stresses occur in a larger region around the center.

We depict the stress evolution within the silicon core during cycling in the normal direction in Figure 4(c) and in the tangential direction in Figure 4(d). As discussed for the SEI mechanics, the normal stress inside silicon at the boundary is approximately 100 times larger compared to the soft SEI scenario with a similar shape of the stress profile. The tangential stress inside silicon is compressive during lithiation and changes to tensile stress during delithiation analog to the soft SEI case. However, the largest tangential stress magnitudes appear at point **LR** in contrast to the scenario with the soft SEI, where the largest tangential stress magnitude appears at point **UL**. Thus, the maximum stress magnitudes inside silicon occur at the same point **LR** for the normal and tangential component due to the impact of the stiff SEI shell, which is most significant at this point due to the largest curvature. This effect emphasizes the importance of the mechanical interplay between the silicon core and the SEI shell.

Next, we discuss the influence of the stiff SEI mechanics on the lithiation behavior of the silicon nanowire core. We depict the lithium concentration distribution during lithi-
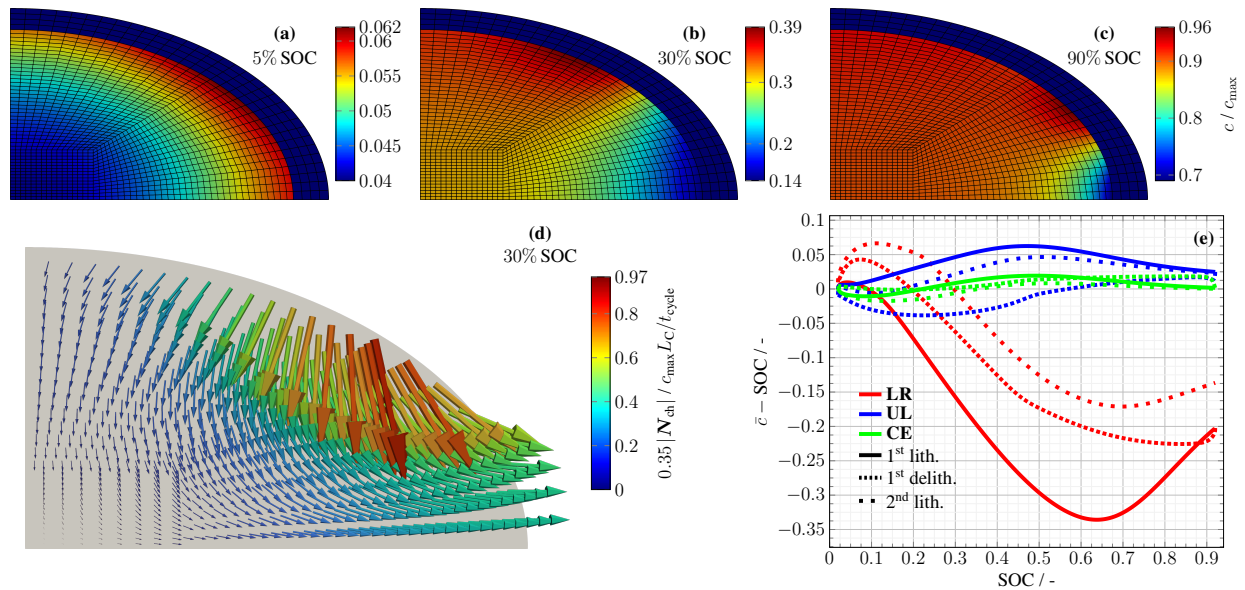
Figure 5. Lithium concentration for the elliptical silicon nanowire with a stiff SEI. Distribution of the lithium concentration inside silicon during lithiation at (a) 5%, (b) 30%, and (c) 90% SOC. (d) Concentration-driven diffusive lithium flux N_{ch} scaled with 0.35. (e) Deviation of the lithium concentration from the mean at the points **LR**, **UL**, and **CE** during three half cycles.

ation in Figure 5 at (a) 5%, (b) 30%, and (c) 90% SOC. The illustration reveals that upon the start of the lithiation, lithium concentration increases at the outer boundary of the silicon core, proceeding gradually towards the center as expected. Nevertheless, this trend is broken during further lithiation, and a concentration anomaly occurs at the end of the major half-axis at point **LR**. The concentration-driven diffusive lithium flux N_{ch} during lithiation at 30% SOC depicted as arrows in Figure 5(d) indicates the negatively scaled concentration gradient and confirms the concentration depletion at point **LR**. This is in contrast to the concentration anomaly found for the soft SEI case at the end of the minor half-axis at point **UL**, where no anomaly occurs for the stiff SEI case. Instead, the anomaly appears at the point with the largest curvature and the most significant stress magnitude generated by the stiff SEI. Again, the stress-driven convective lithium flux N_{el} depicted in Figure 9(b) guarantees that the total lithium flux N always points towards the interior of the silicon core during lithiation. This confirms the importance of the chemo-mechanical interplay and the severe influence of the stiff SEI shell on the lithiation behavior of the silicon nanowire core. The stiff SEI shell acts similarly to a rigid obstacle hindering local volume expansion and, consequently, lithiation as discussed in Ref. [33].

We depict the evolution of the lithium concentration in Figure 5(e) to estimate the robustness of the mechanical impact during cycling. During the first lithiation, the decrease in concentration at point **LR** exists in the whole SOC range. During the subsequent delithiation, this decrease in concentration reduces continuously, and an increase in concentration, meaning an anomaly, appears for SOC values smaller than 20%. During the second lithiation, a concentration anomaly appears for SOC values larger than 30%. The second lithiation deviates significantly from the first lithiation due to the viscoplastic behavior of the SEI shell. Nevertheless, the concentration anomaly caused by the mechanical impact of the stiff SEI shell is a robust effect appearing during every cycle.

The stiff SEI mechanics influences the chemo-mechanical potential inside silicon. Due to the viscoplastic behavior, the stiff SEI shell generates a stress hysteresis during cycling, causing a voltage hysteresis as depicted in Figure 12. Thus, the hysteresis effect discussed in Refs. [26, 27] for a spherical silicon particle covered by a stiff SEI shell also occurs for elliptical nanowires. This demonstrates the importance of mechanical considerations for silicon cores and SEI shells in simulations dealing with silicon anodes as battery active material.

5. Summary and Conclusion

In this study, we have systematically investigated the mechanical behavior and lithiation characteristics of an elliptical silicon nanowire core covered by a viscoplastic SEI shell with a 2D chemo-mechanical simulation. We have compared the influence of a soft and stiff SEI shell on the system and discussed the effect of the elliptical geometry. We base our model and numerical simulation on a higher order finite element method with a variable-step, variable-order time integration scheme extended straightforwardly from the 1D radial symmetric case [29].

Concerning the mechanics, the silicon and soft SEI system shows the largest stress magnitudes in tangential direction at the end of the minor half-axis at point **UL**, where the curvature is minor. The normal component of the stress shows the largest magnitude at the end of the major half-axis at point **LR**, however, with significantly smaller values compared to the tangential stresses. For the stiff SEI case, the system reaches the largest stress magnitudes at the end of the major half-axis at point **LR**, where the curvature is major and the mechanical impact of the SEI is dominant. Thus, the stress magnitudes are significantly higher compared to the soft SEI case. Only the tangential stress component inside the SEI is larger at the point with the smallest curvature **UL**, where the SEI is prone to cracking. Symmetric silicon nanowires with the same capacity and

corresponding SEI shell are mechanically more stable than elliptical nanowires.

The mechanics of the elliptical geometry significantly influences the lithiation behavior of the silicon nanowire. Generally, the lithium concentration is increased at the outer boundary during lithiation and decreased during delithiation, with the fastest concentration changes at the end of the major half-axis at point **LR** due to the largest surface-to-volume ratio at this point. For the soft SEI case, the concentration distribution reveals a deviation from this trend at the end of the minor half-axis at point **UL**. This concentration anomaly also appears during slow cycling and without SEI. Therefore, the mechanics of the elliptical silicon nanowire causes this effect. For the stiff SEI case, in contrast, a concentration anomaly occurs at the end of the major half-axis at point **LR**. The SEI influences the lithiation behavior more dominantly at this point due to the pronounced curvature. In total, the soft SEI has only a minor effect on the silicon nanowire, while the stiff SEI significantly impacts the lithiation behavior.

As shown in Refs. [56–58], inhomogeneous lithiation on particle scale is also responsible for considerable overpotential fluctuations on electrode scale. Our results demonstrate that inclusion of mechanical effects not only predicts mechanical degradation but also influences electrochemically induced degradation due to the mechanically induced overpotential fluctuations.

To conclude, we have demonstrated the importance of the chemo-mechanical coupling, the geometry, and the SEI on the silicon anode behavior during cycling. Based on our work, further simulations could include plasticity of the silicon nanowire, fracture modes inside silicon and SEI, or SEI growth. From a numerical perspective, an adaptive spatial grid algorithm could optimize the simulation.

Acknowledgements

Conflict of Interest

The authors declare that they have no known competing financial interests or personal relationships that could have appeared to influence the work in this paper.

CRediT authorship contribution statement

R. Schoof: Conceptualization, Methodology, Software, Validation, Formal analysis, Investigation, Data Curation, Writing – Original Draft, Visualization. **L. Köbbing:** Conceptualization, Methodology, Validation, Formal analysis, Investigation, Writing – Original Draft, Visualization. **A. Latz:** Resources, Writing – Review & Editing, Project administration, Funding acquisition. **B. Horstmann:** Resources, Writing – Review & Editing, Supervision. **W. Dörfler:** Resources, Writing – Review & Editing, Supervision, Project administration, Funding acquisition.

ORCID

R. Schoof: 0000-0001-6848-3844, L. Köbbing: 0000-0002-1806-6732, A. Latz: 0000-0003-1449-8172, B. Horstmann: 0000-0002-1500-0578, W. Dörfler: 0000-0003-1558-9236

References

[1] M. N. Obrovac, V. L. Chevrier, *Chem. Rev.* **2014**, *114*, 11444–11502, DOI 10.1021/cr500207g.

[2] L. Sun, Y. Liu, R. Shao, J. Wu, R. Jiang, Z. Jin, *Energy Storage Mater.* **2022**, *46*, 482–502, DOI 10.1016/j.ensm.2022.01.042.

[3] X. Zuo, J. Zhu, P. Müller-Buschbaum, Y.-J. Cheng, *Nano Energy* **2017**, *31*, 113–143, DOI 10.1016/j.nanoen.2016.11.013.

[4] K. Feng, M. Li, W. Liu, A. G. Kashkooli, X. Xiao, M. Cai, Z. Chen, *Small* **2018**, *14*, DOI 10.1002/smll.201702737.

[5] Y. Li, Q. Li, J. Chai, Y. Wang, J. Du, Z. Chen, Y. Rui, L. Jiang, B. Tang, *ACS Materials Lett.* **2023**, *5*, 2948–2970, DOI 10.1021/acsmaterialslett.3c00253.

[6] L. Y. Beaulieu, K. W. Eberman, R. L. Turner, L. J. Krause, J. R. Dahn, *Electrochemical and Solid-State Letters* **2001**, *4*, A137, DOI 10.1149/1.1388178.

[7] N. Kim, Y. Kim, J. Sung, J. Cho, *Nature Energy* **2023**, *8*, 921–933, DOI 10.1038/s41560-023-01333-5.

[8] X. H. Liu, L. Zhong, S. Huang, S. X. Mao, T. Zhu, J. Y. Huang, *ACS Nano* **2012**, *6*, 1522–1531, DOI 10.1021/nn204476h.

[9] M. Wetjen, S. Solchenbach, D. Pritzl, J. Hou, V. Tileli, H. A. Gasteiger, *J. Electrochem. Soc.* **2018**, *165*, A1503–A1514, DOI 10.1149/2.1261807jes.

[10] X. Su, Q. Wu, J. Li, X. Xiao, A. Lott, W. Lu, B. W. Sheldon, J. Wu, *Adv. Energy Mater.* **2014**, *4*, 1–23, DOI 10.1002/aenm.201300882.

[11] Y. Yang, W. Yuan, W. Kang, Y. Ye, Y. Yuan, Z. Qiu, C. Wang, X. Zhang, Y. Ke, Y. Tang, *Nanoscale* **2020**, *12*, 7461–7484, DOI 10.1039/C9NR10652A.

[12] L. Xu, *J. Phys. Conf. Ser.* **2023**, *2608*, 012001, DOI 10.1088/1742-6596/2608/1/012001.

[13] C. K. Chan, H. Peng, G. Liu, K. McIlwrath, X. F. Zhang, R. A. Huggins, Y. Cui, *Nat. Nanotechnol.* **2008**, *3*, 31–35, DOI 10.1038/nnano.2007.411.

[14] Y. Yang, W. Yuan, W. Kang, Y. Ye, Q. Pan, X. Zhang, Y. Ke, C. Wang, Z. Qiu, Y. Tang, *Sustain. Energy Fuels* **2020**, *4*, 1577–1594, DOI 10.1039/C9SE01165J.

[15] F. Kilchert, M. Schammer, A. Latz, B. Horstmann, *Energy Technol.* **2024**, *n/a*, 2400206, DOI 10.1002/ente.202400206.

[16] B. Horstmann, F. Single, A. Latz, *Curr. Opin. Electrochem.* **2019**, *13*, 61–69, DOI 10.1016/j.coelec.2018.10.013.

[17] X. Zhang, S. Weng, G. Yang, Y. Li, H. Li, D. Su, L. Gu, Z. Wang, X. Wang, L. Chen, *Cell Rep. Phys. Sci.* **2021**, *2*, 100668, DOI 10.1016/j.xcrp.2021.100668.

[18] H. Adenusi, G. A. Chass, S. Passerini, K. V. Tian, G. Chen, *Adv. Energy Mater.* **2023**, *13*, DOI 10.1002/aenm.202203307.

[19] A. Wang, S. Kadam, H. Li, S. Shi, Y. Qi, *npj Comput. Mater.* **2018**, *4*, DOI 10.1038/s41524-018-0064-0.

[20] L. von Kolzenberg, A. Latz, B. Horstmann, *ChemSusChem* **2020**, *13*, 3901–3910, DOI 10.1002/cssc.202000867.

[21] L. Köbbing, A. Latz, B. Horstmann, *J. Power Sources* **2023**, *561*, 232651, DOI 10.1016/j.jpowsour.2023.232651.

[22] Y.-X. Yao, J. Wan, N.-Y. Liang, C. Yan, R. Wen, Q. Zhang, *J. Am. Chem. Soc.* **2023**, *145*, 8001–8006, DOI 10.1021/jacs.2c13878.

[23] Y. Zhang, N. Du, D. Yang, *Nanoscale* **2019**, *11*, 19086–19104, DOI 10.1039/C9NR05748J.

[24] L. von Kolzenberg, A. Latz, B. Horstmann, *Batter. Supercaps* **2022**, *5*, 1–12, DOI 10.1002/batt.202100216.

[25] K. Guo, R. Kumar, X. Xiao, B. W. Sheldon, H. Gao, *Nano Energy* **2020**, *68*, 104257, DOI 10.1016/j.nanoen.2019.104257.

[26] L. Köbbing, A. Latz, B. Horstmann, *Adv. Funct. Mater.* **2024**, *34*, 2308818, DOI 10.1002/adfm.202308818.

[27] L. Köbbing, Y. Kuhn, B. Horstmann, *ArXiv* **2024**, DOI 10.48550/arXiv.2408.01106.

[28] D. Wycisk, G. K. Mertin, M. Oldenburger, O. von Kessel, A. Latz, *J. Energy Storage* **2024**, *89*, 111617, DOI 10.1016/j.est.2024.111617.

[29] R. Schoof, G. F. Castelli, W. Dörfler, *Examples Counterexamples* **2024**, Accepted: 30.08.2024, ArXiV: 10.48550/arXiv.2404.01884, DOI 10.1016/j.exco.2024.100157.

[30] G. F. Castelli, L. von Kolzenberg, B. Horstmann, A. Latz, W. Dörfler, *Energy Technol.* **2021**, *9*, 2000835, DOI 10.1002/ente.202000835.

[31] R. Schoof, J. Niermann, A. Dyck, T. Böhlke, W. Dörfler, *Comput. Mech.* **2024**, DOI 10.1007/s00466-024-02499-9.

[32] R. Schoof, G. F. Castelli, W. Dörfler in 8th European Congress on Computational Methods in Applied Sciences and Engineering (ECCOMAS Congress 2022), (Eds.: T. Kvamsdal, K. M. Mathisen, K.-A. Lie, M. G. Larson), CIMNE, Barcelona, **2022**, DOI 10.23967/eccomas.2022.106.

[33] R. Schoof, G. F. Castelli, W. Dörfler, *Comput. Math. Appl.* **2023**, *149*, 135–149, DOI 10.1016/j.camwa.2023.08.027.

[34] M. Tanaka, J. B. Hooper, D. Bedrov, *ACS Appl. Energy Mater.* **2018**, *1*, 1858–1863, DOI 10.1021/acsaem.8b00344.

[35] J. Ding, X. Li, L. Gong, P. Tan, *Advanced Powder Materials* **2024**, *3*, 100200, DOI 10.1016/j.apmate.2024.100200.

[36] R. Schoof, L. Flür, F. Tuschner, W. Dörfler, *Springer Proc. Math. Stat.* **2024**, Accepted: 15.03.2024, DOI 10.48550/arXiv.2401.10135.

[37] M. Schammer, B. Horstmann, A. Latz, *J. Electrochem. Soc.* **2021**, *168*, 026511, DOI 10.1149/1945-7111/abdddf.

[38] T. Zhang, M. Kamlah, *J. Electrochem. Soc.* **2018**, *165*, A1997–A2007, DOI 10.1149/2.0141810jes.

[39] A. Bertram, *Elasticity and Plasticity of Large Deformations: Including Gradient Materials*, 4th ed., Springer Nature Switzerland AG, Cham, **2021**, DOI 10.1007/978-3-030-72328-6.

[40] J. Lubliner, *Plasticity theory*, Pearson Education, Inc., New York, **2006**, DOI 10.1115/1.2899459.

[41] C. V. Di Leo, E. Rejovitzky, L. Anand, *Int. J. Solids Struct.* **2015**, *67-68*, 283–296, DOI 10.1016/j.ijsolstr.2015.04.028.

[42] G. A. Holzapfel, *Nonlinear Solid Mechanics*, John Wiley & Sons, Ltd., Chichester, **2010**.

[43] L. Anand, *J. Mech. Phys. Solids* **2012**, *60*, 1983–2002, DOI 10.1016/j.jmps.2012.08.001.

[44] C. V. Di Leo, PhD thesis, Massachusetts Institute of Technology (MIT), **2015**.

[45] J. C. Simo, T. J. R. Hughes, *Computational inelasticity*, Springer, New York, **1998**.

[46] E. L Wilson, *Int. J. Numer. Methods Eng.* **1974**, *8*, 198–203, DOI 10.1002/nme.1620080115.

[47] D. A. Di Pietro, A. Ern, *Comput. Methods Appl. Mech. Engrg.* **2015**, *283*, 1–21, DOI 10.1016/j.cma.2014.09.009.

[48] D. Braess, *Finite Elements*, Third, Cambridge University Press, Cambridge, **2007**, DOI 10.1007/978-3-540-72450-6.

[49] M. W. Reichelt, L. F. Shampine, J. Kierzenka, MATLAB ode15s, Copyright 1984–2020 The MathWorks, Inc., **1997**.

[50] L. F. Shampine, M. W. Reichelt, *SIAM J. Sci. Comput.* **1997**, *18*, 1–22, DOI 10.1137/S1064827594276424.

[51] L. F. Shampine, M. W. Reichelt, J. A. Kierzenka, *SIAM Rev.* **1999**, *41*, 538–552, DOI 10.1137/S0036144598334254X.

[52] T. A. Davis, *ACM Trans. Math. Software* **2004**, *30*, 196–199, DOI 10.1145/992200.992206.

[53] D. Arndt, W. Bangerth, M. Bergbauer, M. Feder, M. Fehling, J. Heinz, T. Heister, L. Heltai, M. Kronbichler, M. Maier, P. Munch, J.-P. Pelteret, B. Turcksin, D. Wells, S. Zampini, *J. Numer. Math.* **2023**, *31*, 231–246, DOI 10.1515/jnma-2023-0089.

[54] WIKI bw HPC Team, BwUniCluster 2.0 Hardware and Architecture, **2024**.

[55] M. Huttin, PhD thesis, Karlsruher Institut für Technologie (KIT), Karlsruhe, **2014**, DOI 10.5445/IR/1000039883.

[56] I. Traskunov, A. Latz, *Electrochim. Acta* **2021**, *379*, 138144, DOI 10.1016/j.electacta.2021.138144.

[57] I. Traskunov, A. Latz, *Energy Technol.* **2021**, *9*, 16–19, DOI 10.1002/ente.202000861.

[58] I. Traskunov, A. Latz, *Electrochim. Acta* **2022**, *434*, 141248, DOI 10.1016/j.electacta.2022.141248.

[59] C. K. Chan, H. Peng, G. Liu, K. McIlwrath, X. F. Zhang, R. A. Huggins, Y. Cui, *Nat. Nanotechnol.* **2007**, *3*, 31–35, DOI 10.1038/nnano.2007.411.

Appendices

A. Symmetric Nanowire with Soft SEI

For comparison, we investigate the stresses and the lithiation characteristics of a symmetric silicon nanowire during cycling. We choose the radius as $L_C = 38.73 \cdot 10^{-9}$ m to obtain the same capacity as for the elliptical nanowire and the thickness of the SEI is chosen as an eighth of the core length as $L_S = 4.84 \cdot 10^{-9}$ m.

We depict the stress distribution during lithiation at 30% SOC for the normal and tangential component in Figure 6(a) and (b). Inside the silicon core, both components show compressive stresses close to the outer boundary and tensile stresses close to the center. Inside the SEI, the normal stress is compressive close to the nanowire and vanishes at the outer boundary. The tangential component is tensile inside the whole SEI shell.

We show the evolution of the stress components at the interface during three half-cycles in Figure 6(c), (d), and (e). During lithiation, the normal component and the tangential component inside the silicon core show compressive stress, while the tangential component inside the SEI shell shows tensile stress. Stresses are opposite during delithiation. During the second lithiation, the normal stress inside the silicon and the tangential stress inside the SEI converge gradually to the stress during the first lithiation. The tangential stress inside the silicon during the second lithiation coincides with the first
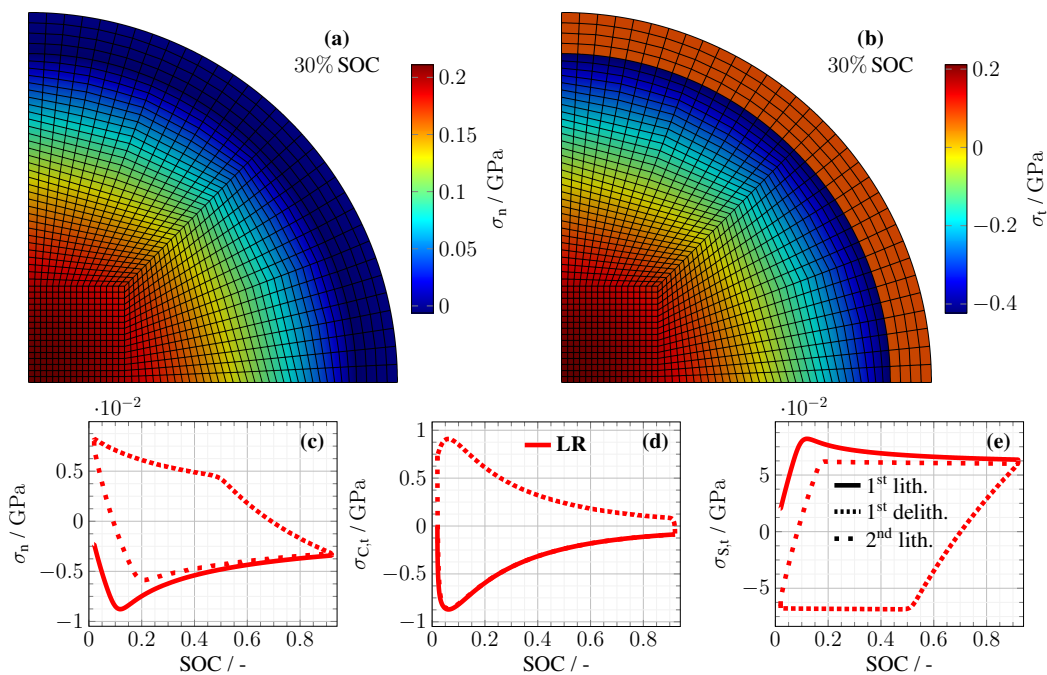

Figure 6. Cauchy stresses for the symmetric silicon nanowire with a soft SEI. Distribution of (a) normal and (b) tangential Cauchy stress inside the silicon core and the SEI shell during lithiation at 30% SOC. Evolution of Cauchy stress at the interface during three half cycles for (c) normal, (d) tangential core, and (e) tangential shell stress.
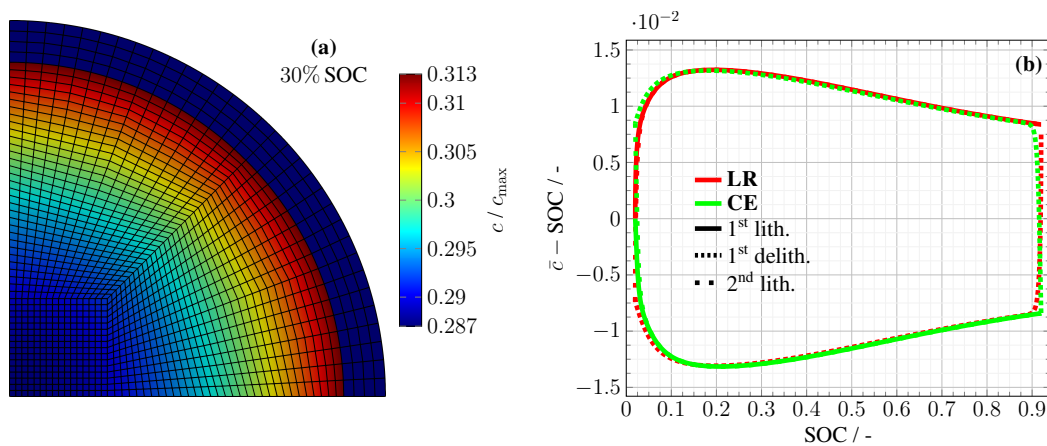

Figure 7. Lithium concentration for the symmetric silicon nanowire with a soft SEI. (a) Distribution of the lithium concentration inside silicon during lithiation at 30% SOC. (b) Deviation of the lithium concentration from the mean at the interface **LR** and the center **CE** during three half cycles.

lithiation for the whole SOC range. The stress magnitude is always smaller than the maximum magnitude in the elliptical case.

In Figure 7(a), we depict the concentration distribution within the symmetric silicon nanowire during lithiation at 30% SOC. The concentration increases from the outer boundary during lithiation and no concentration anomaly occurs. The deviation of the lithium concentration at the outer boundary and the center from the mean during cycling is shown in Figure 7(b). As expected, during lithiation, the lithium concentration at the outer boundary exceeds the mean, while the concentration at the center is smaller than the mean. The concentration profiles are vice versa during delithiation, as expected.

B. Variation of Plastic Strain Rate $\dot{\varepsilon}_0$

To estimate the influence of the viscoplastic behavior, we vary the plastic strain rate $\dot{\varepsilon}_0$ for the soft SEI. For higher values, plastic flow starts quickly upon reaching the yield condition, while it starts only slowly for smaller values. We depict the normal component of the stress inside the SEI shell in Figure 8(a) and the tangential component in Figure 8(b). The magnitude of both stress components and the size of the stress overshoot increase with decreasing plastic strain rate $\dot{\varepsilon}_0$. This is expected due to the retarded plastic flow for low plastic strain rates $\dot{\varepsilon}_0$. Nevertheless, the stress profiles reveal a similar shape for all tested values. For our simulations, we take the medium parameter $\dot{\varepsilon}_0 = 10^{-5}\,\mathrm{s}^{-1}$.
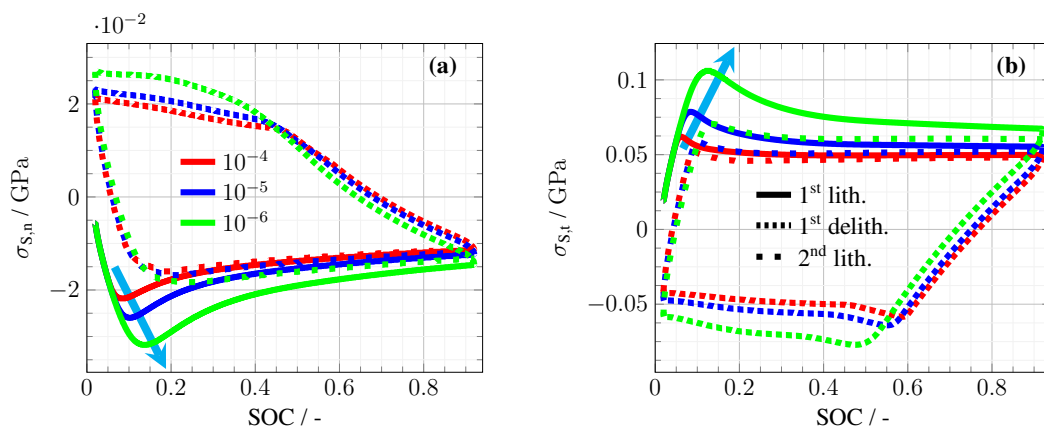

Figure 8. Variation of the plastic strain rate $\dot{\varepsilon}_0$ for the soft SEI. Evolution of the Cauchy stress inside the SEI during cycling for (a) the normal and (b) the tangential stress component.

C. Stress-Driven Lithium Flux N_el

We depict the stress-driven convective lithium flux $\boldsymbol{N}_\mathrm{el}$ during lithiation at 30% SOC in Figure 9 to complement the illustrations of the concentration-driven diffusive lithium flux $\boldsymbol{N}_\mathrm{ch}$ in Figure 3(d) and Figure 5(d). For the soft SEI case shown in Figure 9(a), the stress-driven lithium flux everywhere points towards the interior of the silicon core. The largest magnitude of the stress-driven flux occurs at point **UL**, where the largest stress values and stress gradients exist. For the stiff SEI case shown in Figure 9(b), the stress-driven lithium flux mostly points towards the interior of the silicon core. The largest magnitude of the stress-driven flux and a significant deviation from center-directed flux occurs at the outer boundary in a larger region around point **LR**, where the largest stress values and stress gradients exist. Combining both flux components, the total lithium flux always points towards the interior of the silicon core during lithiation for the soft SEI as well as for the stiff SEI.
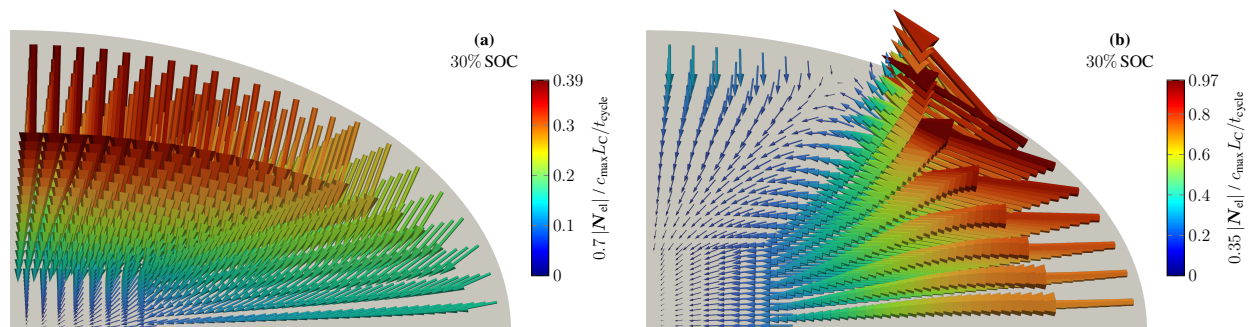

Figure 9. Stress-driven convective lithium flux $\boldsymbol{N}_\mathrm{el}$ for (a) the soft SEI case and (b) the stiff SEI case with different scaling for the fluxes.

D. Silicon Nanowire without SEI and C/20

We briefly investigate the stress and lithiation characteristics of an elliptical silicon nanowire without SEI during slow cycling with C/20 to estimate the influence of the SEI and the C-rate. The stress distribution in normal direction during lithiation at 30% SOC is depicted in Figure 10(a). The normal component vanishes at the outer boundary due to the surface condition and shows tensile stress throughout the nanowire. The largest stress magnitude is achieved close to the center along the major half-axis. We display the tangential stress component in Figure 10(b). The tangential component shows compressive stress at the outer boundary, with the largest magnitude occurring at the end of the minor half-axis at point **UL**. The tangential stress is tensile in a region around the center. In Figure 10(c), we depict the evolution of the tangential Cauchy stress during cycling at the points **LR** and **UL**. The curves reveal compressive stress during lithiation and tensile stress during delithiation. The largest stress magnitudes occur at the end of the minor half-axis at point **UL** for the whole SOC range. The stress distribution and evolution during slow cycling is similar to the soft SEI case and cycling with 1 C. Only the magnitude of the stresses is smaller in general due to the reduced C-rate.

In Figure 11, we display the lithium concentration distribution during lithiation at (a) 5%, (b) 30%, and (c) 90% SOC. The concentration shows the largest values at the end of the major half-axis at point **LR** due to the highest surface-to-volume ratio at this point. At 30% SOC, the distribution shows a concentration depletion at the end of the minor half-axis at point **UL**. The negatively scaled concentration gradient during lithiation at 30% SOC in Figure 11(d) indicates the chemical diffusion component of the lithium flux and illustrates the anomaly at point **UL**. In Figure 11(e), we depict the deviation of the lithium concentration at the points **LR**, **UL**, and **CE** from the mean during cycling. The evolution reveals the pronounced concentration increase/decrease at point **LR** during lithiation/delithiation. Furthermore, the evolution reveals the concentration anomaly at point **UL** during cycling between 10% and 40% SOC. In total, the lithiation characteristics during slow cycling without SEI are similar to standard cycling with SEI. Only the magnitude of the concentration deviations is significantly reduced due to the smaller C-rate.
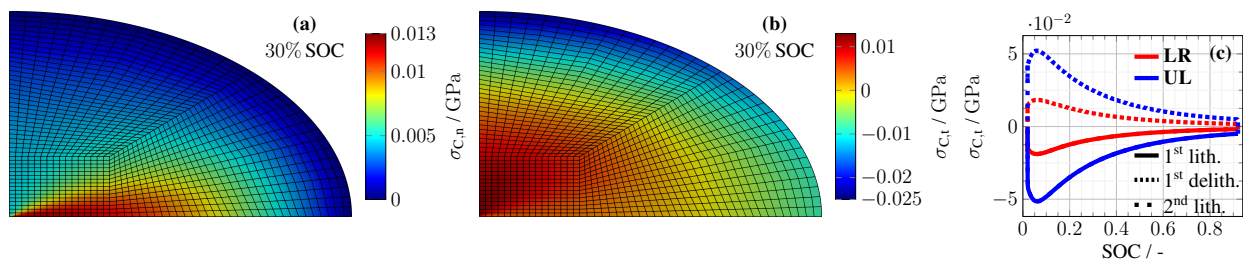

Figure 10. Cauchy stresses for the elliptical silicon nanowire without SEI during cycling with C/20. Distribution of (a) normal and (b) tangential Cauchy stress inside the silicon core during lithiation at 30% SOC. (c) Evolution of the tangential Cauchy stress at the points **LR** and **UL** during three half cycles.
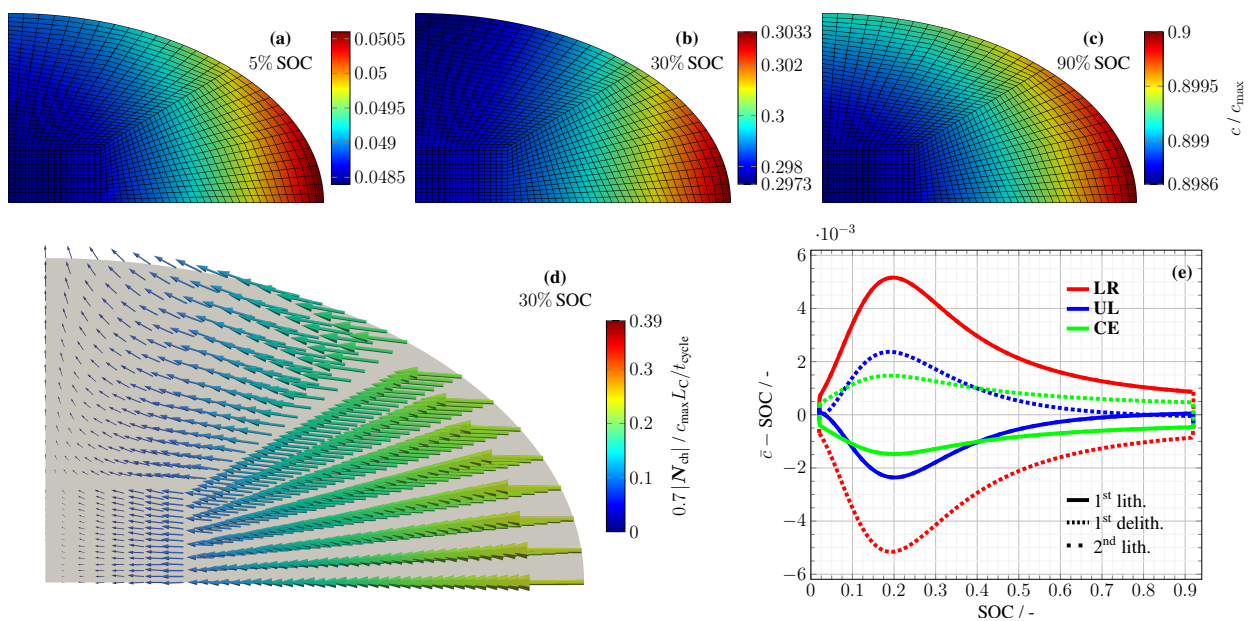

Figure 11. Concentration for silicon nanowire only with C/20. Lithium concentration for the elliptical silicon nanowire without SEI during cycling with C/20. Distribution of the lithium concentration inside silicon during lithiation at (a) 5%, (b) 30%, and (c) 90% SOC. (d) Concentration-driven diffusive lithium flux N_{ch} scaled with 0.7. (e) Deviation of the lithium concentration from the mean at the points **LR**, **UL**, and **CE** during three half cycles.

E. Voltage Hysteresis

To estimate the mechanical impact of the SEI shell on the lithiation behavior of the silicon nanowire, we compare the voltage during slow cycling with C/20 with the soft and the stiff SEI shell. Due to numerical reasons, we adjust the plastic strain rate to $\dot{\varepsilon}_0 = 10^{-6}\,\mathrm{s}^{-1}$. For both cases depicted in Figure 12, the voltages at point **LR** and **UL** are equivalent, revealing chemo-mechanical equilibrium during slow cycling. For the soft SEI case displayed in Figure 12(a), also the voltages during lithiation and delithiation coincide. In contrast, Figure 12(b) reveals that a voltage hysteresis arises for the stiff SEI case. This is in agreement with our explanation of the voltage hysteresis for spherical silicon nanoparticles covered by a stiff SEI shell presented in Refs. [26, 27].
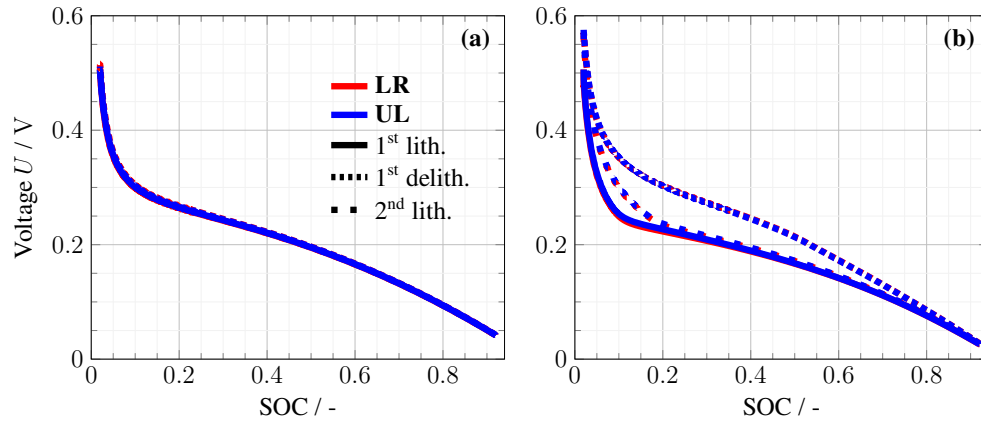

Figure 12. Voltage for the elliptical silicon nanowire covered by SEI during slow cycling with C/20 for (a) soft and (b) stiff SEI.

F. Table with Parameters

The simulation parameters and constants are summarized in Table 1. Additionally, we follow Ref. [24] and use $U_{\mathrm{max}} = 0.5\,\mathrm{V}$ and $U_{\mathrm{min}} = 0.05\,\mathrm{V}$ as maximal and minimal voltage for the lithiation and delithiation. Therefore, we choose $\bar{c}_0 = 0.02$ as constant initial concentration and $0.9\,\mathrm{h}$ as duration of one half cycle. The applied OCV curve

$$U_{\mathrm{OCV}}(\bar{c}) = \frac{-0.2453\,\bar{c}^3 - 0.00527\,\bar{c}^2 + 0.2477\,\bar{c} + 0.006457}{\bar{c} + 0.002493} \tag{5}$$

is delivered by Ref. [59].

Table 1. Model parameters for the numerical experiments [24, 31, 41].

Description	Symbol	Value	Unit	Dimensionless
Universal gas constant	R_{gas}	8.314	$\mathrm{J\,mol^{-1}\,K^{-1}}$	1
Faraday constant	F	96485	$\mathrm{J\,V^{-1}\,mol^{-1}}$	1
Operation temperature	T	298.15	K	1
Silicon				
Core length scale	L_{C}	$50 \cdot 10^{-9}$	m	1
Cycle time	t_{cycle}	3600	s	1
Diffusion coefficient	D	$1 \cdot 10^{-17}$	$\mathrm{m^2\,s^{-1}}$	14.4
OCV curve	U_{OCV}	Equation (5)	V	$F/R_{\mathrm{gas}}T \cdot (5)$
Young's modulus	E_{C}	$90.13 \cdot 10^{9}$	Pa	116.74
Partial molar volume	v_{pmv}	$10.96 \cdot 10^{-6}$	$\mathrm{m^3\,mol^{-1}}$	3.41
Maximal concentration	c_{max}	$311.47 \cdot 10^{3}$	$\mathrm{mol\,m^{-3}}$	1
Initial concentration	c_0	$6.23 \cdot 10^{3}$	$\mathrm{mol\,m^{-3}}$	$2 \cdot 10^{-2}$
Poisson's ratio	ν_{C}	0.22	–	0.22
SEI				
Shell length scale	L_{S}	$6.25 \cdot 10^{-9}$	m	0.125
Young's modulus	E_{S}	$900 \cdot 10^{6}$	Pa	1.17
Poisson's ratio	ν_{S}	0.25	–	0.25
Yield stress	σ_{Y}	$49.5 \cdot 10^{6}$	Pa	0.052
Strain measurement	β	2.94	–	2.94
Stress constant	σ_{Y^*}	$49.5 \cdot 10^{6}$	Pa	0.052
Tensile plastic strain rate	$\dot{\varepsilon}_0$	$1.0 \cdot 10^{-5}$	$\mathrm{s^{-1}}$	0.036